chemosensors

MDPI

Article

A Laser-Printed Surface-Enhanced Photoluminescence Sensor for the Sub-Nanomolar Optical Detection of Mercury in Water

Yulia Borodaenko [1], Stanislav Gurbatov [1,2], Evgeny Modin [3], Aleksandr Chepak [4], Mikhail Tutov [2,4], Aleksandr Mironenko [4,*] and Aleksandr Kuchmizhak [1,2,*]

[1] Institute of Automation and Control Processes, Far Eastern Branch, Russian Academy of Science, 5 Radio Str., Vladivostok 690041, Russia
[2] Department of Chemistry and Materials, Far Eastern Federal University, 10 Ajax Bay, Russky Island, Vladivostok 690922, Russia
[3] CIC NanoGUNE BRTA, 76 Avda Tolosa, 20018 Donostia-San Sebastian, Spain
[4] Institute of Chemistry, Far Eastern Branch, Russian Academy of Sciences, 159 Prosp. 100-letiya Vladivostoka, Vladivostok 690022, Russia
* Correspondence: almironenko@gmail.com (A.M.); alex.iacp.dvo@mail.ru (A.K.)

Abstract: Here, we report a novel, easy-to-implement scalable single-step procedure for the fabrication of a solid-state surface-enhanced photoluminescence (SEPL) sensor via the direct femtosecond (fs) laser patterning of monocrystalline Si wafers placed under the layer of functionalizing solution simultaneously containing a metal salt precursor ($AgNO_3$) and a photoluminescent probe (d114). Such laser processing creates periodically modulated micro- and nanostructures decorated with Ag nanoparticles on the Si surface, which effectively adsorbs and retains the photoluminescent sensor layer. The SEPL effect stimulated by the micro- and nanostructures formed on the Si surface localizing pump radiation within the near-surface layer and surface plasmons supported by the decorating Ag nanoparticles is responsible for the intense optical sensory response modulated by a small amount of analyte species. The produced SEPL sensor operating within a fluidic device was found to detect sub-nanomolar concentrations of Hg^{2+} in water which is two orders of magnitude lower compared to this molecular probe sensitivity in solution. The fabrication technique is upscalable, inexpensive, and flexible regarding the ability to the control surface nano-morphology, the amount and type of loading noble-metal nanoparticles, as well as the type of molecular probe. This opens up pathways for the on-demand development of various multi-functional chemosensing platforms with expanded functionality.

Keywords: hybrid metal–semiconductor nanostructures; laser-induced periodic surface structures; surface-enhanced photoluminescence; luminescence-based sensing; mercury ions

Citation: Borodaenko, Y.; Gurbatov, S.; Modin, E.; Chepak, A.; Tutov, M.; Mironenko, A.; Kuchmizhak, A. A Laser-Printed Surface-Enhanced Photoluminescence Sensor for the Sub-Nanomolar Optical Detection of Mercury in Water. *Chemosensors* **2023**, *11*, 307. https://doi.org/10.3390/chemosensors11050307

Academic Editor: Sofian Kanan

Received: 3 April 2023
Revised: 15 May 2023
Accepted: 18 May 2023
Published: 20 May 2023

1. Introduction

The design and fabrication of solid-state chemical sensors for point -of-care testing, security screening, or ecological monitoring represents an increasingly growing research field. Along with improved sensor performance, demanding sensor designs should address multiple criteria such as inexpensive and green mass production as well as facile miniaturization. Among others, chemoresponsive luminescent materials represent a promising platform for sensor design. Thus, being an almost non-invasive analytical technique, luminescence-based sensing has become an effective analytical tool extensively used in the chemical, biomedical, and diagnostic fields due to its unique capability in terms of the sensitive monitoring of metal ions [1–4], anions [5,6], reactive oxygen species [7,8], and biomolecules [9,10]. This approach combines the benefits of real-time analysis with in situ detection [11]; however, the common solid state luminophores such as quantum dots [12,13], polymers [14,15], or organic dyes [16,17] suffer the shortcomings of low luminescence quantum efficiency and having a small extinction coefficient [18–21], which severely limits applications of these materials in the form of thin solid films for the highly sensitive detection of analytes.

Inherently weak optical signals from quantum emitters can be empowered by placing them onto specially designed substrates via a phenomenon referred to as surface-enhanced photoluminescence (SEPL). SEPL originates from the interaction between light, luminescent species, and optically resonant nanostructures made of plasmon-supporting noble metals [22] or high-index low-loss semiconductors (such as Si and Ge) [23–27]. This technique has received wide attention in recent years due to a significant improvement in sensing performance as a result of the ability to reliably detect an analytical signal from a small number of quantum emitters, which in some cases can give single-molecule sensitivity [28]. Hybrid combinations of plasmon-active nanoparticles and lossless semiconductors allowing to bring the benefits of both concepts into the unified nanostructures hold promise for the development of advanced sensing platforms with expanded functionality and outstanding performance [29–32]; however, practical realization and replication of such hybrid nanostructures and related sensing devices requires complex multi-step production chains (such as the application of photoresist, exposure, etching, etc. [33]) making the resulting sensing platforms too expensive for routine applications. Moreover, applying an emitting sensitive layer onto the hybrid nanostructures via chemical or physical processes adds another complicated link to the production chain of efficient chemical sensing platforms.

In this paper, we demonstrate an easy-to-implement scalable single-step procedure of SEPL sensor fabrication via direct femtosecond (fs) laser patterning of monocrystalline Si wafers in a functionalizing solution simultaneously containing a metal salt precursor ($AgNO_3$) and a photoluminescent probe (d114) sensitive to the trace concentrations of mercury ions (Hg^{2+}). The laser-induced periodic surface structuring of the Si wafer results in the formation of a nanograting, while localized thermal decomposition of the $AgNO_3$ precursor decorates the obtained hierarchical surface morphology with plasmon-active nanoparticles. The produced hybrid nanotextured surfaces exhibit good wettability, facilitating preferential deposition of d114 molecules directly from the functionalizing solution that finalizes the SEPL sensor fabrication. The SEPL sensor areas were comprehensively characterized by transmission electron microscopy (TEM) and optical and photoluminescence spectroscopy, confirming localized laser-assisted decoration of Si nanogratings by Ag nanoparticles and enhanced PL signals from the attached d114 probe molecules. The produced SEPL sensor operating within a fluidic device was found to detect sub-nanomolar concentrations of Hg^{2+}, improving the detection limit of the d114 probe used in the solution by two orders of magnitude.

2. Materials and Methods

2.1. Chemicals and Instruments

Rhodamine 6G (99%, Sigma Aldrich, St. Louis, MO, USA), silver nitrate (Sigma-Aldrich, St. Louis, MO, USA, 99%), 4-(dimethylamino)benzaldehyde (99%, Sigma Aldrich, St. Louis, MO, USA), Lawesson reagent 2,4-Bis-(4-methoxyphenyl)-1,3-dithia-2,4-diphosphetane 2,4-disulfide (97%, Sigma Aldrich, St. Louis, MO, USA), hexane (95%, Sigma Aldrich, St. Louis, MO, USA), chloroform (99%, Sigma Aldrich), ethyl acetate (99.8%, Sigma Aldrich), dichloromethane (99%, Sigma Aldrich, St. Louis, MO, USA), hydrazine monohydrate (98%, Sigma Aldrich, St. Louis, MO, USA), and silica gel (100/200 µm) were used as received. All other reagents were of analytical grade and used without purification. All aqueous solutions were prepared using Millipore ® water. The Fourier transform infrared radiation (FT-IR) spectra of the compounds in the range 400–4000 cm^{-1} were recorded using a Perkin Elmer Spectrum 100BX II spectrometer in KBr pellets. The 1H, 13C NMR spectra were performed on a Bruker Avance 400 with the frequency of proton resonance 400 MHz using CDCl3 as the solvent and tetramethylsiliane as the internal reference. Mass spectrometry was performed on a LC-ESI/MS system Shimadzu LCMS-2010.

2.2. Synthesis of the Photoluminescent Probe (d114)

The probe used in the work (d114) was obtained in three successive stages from rhodamine 6 g as we described earlier [19]. ^{1}H NMR (400 MHz, $CDCl_3$, ppm, δ): 8.53 (s, 1H, H(24)), 8.12–8.14 (m, 1H, H(12)), 7.05–7.07 (m, 1H, H(9)), 7.37 (s, 1H, H(18)),7.40 (s, 1H, H(19)), 7.66 (s, 1H, H(15)),7.69 (s, 1H, H(22)), 7.40 (m, 2H, H(10), H(11)), 6.30 (br. s, 2H, H(26), H(30)), 6.62 (br. s, 2H, H(27), H(29)), 3.50 (br.s, 2H, H(33), H(36)), 3.20–3.21 (q, 4H, H(34), H(37)), 3.01 (s, 6H, H(41), H(42)), 1.92 (s, 6H, H(32), H(39)), 1.29–1.33 (t, 6H, H(35), H(38)); ^{13}C NMR (100 MHz, $CDCl_3$, ppm, δ): 14.36, 14.92, 17.02, 22.92, 29.93, 32.15, 38.78, 40.38, 96.75, 111.76, 118.32, 122.32, 127.29, 127.91, 130.39, 130.64, 132.12, 150.20, 152.39, 155.67, 159.72; ESI-MS (m/z, +ve mode) 576.34 $[M + H]^+$, calc. for $C35H38N5OS^+$ is 576.28; Elemental Analysis data: Calc. C, 73.01; H, 6.48; N, 12.16; S, 5.57; Expt. C, 73.33; H, 6.54; N, 12.18; S, 5.41. Mp: 208–210 °C (with decomposition). Detailed information on the synthesis and characterization are provided in the Supplementary Materials.

2.3. Laser Fabrication of the SEPL Sensor

A single-crystal silicon wafer was fixed in a 3 mm quartz cell filled with a transparent functionalizing solution (methanol/H_2O/$AgNO_3$/d114) and directly processed using fs laser pulses (a pulse duration of 200 fs and a central wavelength of 515 nm). Laser radiation was focused onto the Si surface using a dry microscope objective with a numerical aperture of 0.42 through the approx. 3 mm-thick layer of the solution. The cell was placed onto a motorized PC-driven nanopositioning stage allowing precise lateral translation of the sample with respect to the laser spot position. Laser fluence at the output of the microscope objective was controlled by a pyroelectric detector. (A schematic of the experimental setup is presented in Supplementary Materials Figure S2). In all of the experiments, a fixed pulse repetition rate of 1 KHz and a laser scanning speed of 100 um/s were used to avoid excessive heating of the functionalizing solution. After laser processing, the substrate containing the sensitive SEPL spot was successively washed in ethanol and neutral pH deionized water to remove weakly adsorbed precursors and air dried.

2.4. Characterization

The morphology and chemical composition of the laser-patterned Si surface were preliminarily studied using a scanning electron microscope (SEM; Ultra 55+, Carl Zeiss) equipped with an energy-dispersive X-ray (EDX) detector. EDX chemical mapping was carried out at 5 kV acceleration voltage to minimize the penetration depth of the electron beam to the Si bulk increasing signals from the near-surface elements. Focused ion beam milling (FIB; Helios 450, Thermo Fisher, Waltham, MA, USA) was carried out to prepare cross-sectional cuts and 100-nm thick lamella to be further visualized with the transmission electron microscope (TEM; Titan 60–300, Thermo Fisher, Waltham, MA, USA). The milling procedure was performed through the Pt protective layer that was applied over the area of interest using the electron-beam-induced deposition system.

The optical reflectivity of the laser-patterned Ag-decorated Si surface was evaluated using an optical microscope coupled to an optical spectrometer (Shamrock 303i, Andor Technologies, Belfast, UK) with a TE-cooled CCD-camera (Newton, Andor Technologies, Belfast, UK). A microscope objective with a numerical aperture of 0.95 was used to deliver the broadband radiation of the supercontinuum light source to the sample surface and to collect the back-reflected light. A commercial confocal micro-Raman setup (Ntegra Spectra II, NT-MDT) was used to study SEPL effects in the laser-textured surface areas. Linearly polarized CW laser radiation with a wavelength of 473 nm was used to excite the SEPL signal from the d114 adsorbed on the laser-patterned and smooth Si surface areas. The same pump was utilized for confocal mapping of the reflectivity as well as Raman signal distribution over the sample surface. Microscope objectives with NA = 0.28 and 0.7 were used to focus the pump radiation onto the sample surface and to collect reflection, PL, and Raman optical signals that were analyzed with an optical spectrometer (Shamrock 303i, Andor Technologies, Belfast, UK) equipped with a TE-cooled CCD-camera (i-Dus, Andor Technologies, Belfast, UK).

2.5. Sensing Experiments

To examine d114's sensing performance in solution, the probe was dissolved in water/methanol mixture (1/1, v/v; pH = 7.0) to get a 2×10^{-5} M stock solution. Depending on desired concentration of Hg^{2+}, 2–20 μL of 10^{-3} M or 10^{-4} M $HgCl_2$ aqueous solution was added to 2 mL of d114 stock solution and allowed to equilibrate for 60 min at room temperature before measurements. Fluorescence measurements of the solutions were performed on Shimadzu RF-6000 spectrofluorophotometer using 1 cm path length cuvettes at room temperature. To study the optical response of the SEPL sensor, the laser-patterned Si wafer was placed in the fluidic device, allowing for sequential injection of either deionized water containing a calibrated concentration of Hg^{2+} or an EDTA solution (10^{-5} M). The SEPL signal of the d114 probe capping Ag-decorated Si nanograting was excited with a linearly polarized (473 nm) laser pump focused by an objective with NA = 0.1. The same objective collected the PL signal analyzed as a function of the Hg^{2+} concentration with an optical spectrometer (Shamrock 303i, Andor Technologies) with a TE-cooled CCD-camera (Newton, Andor Technologies, Belfast, UK).

3. Results and Discussion

The fabrication procedure of the SEPL sensor with light-emitting molecules attached to the nanoparticle-decorated nanotextured Si surface is schematically illustrated in Figure 1a. The depicted single-step procedure involves direct fs-laser patterning of the monocrystalline Si wafer placed into a transparent functionalizing solution (methanol/H_2O, 10/1, v/v) that contains both the $AgNO_3$ precursor and the d114 probe at millimolar concentrations. Multi-pulse laser exposure at pulse energy below a single-pulse ablation threshold of silicon (F_{th} = 0.13 J/cm^2) causes melting and morphology rearrangement of the near-surface layer. Interference of the incident radiation with its portion coupled to the surface plasma wave creates a periodically modulated intensity pattern imprinted on the Si surface as a nanograting with a characteristic period of about 250 nm and a nano-trench orientation perpendicular with respect to the polarization direction of the laser radiation [34]. The produced morphology represents common laser-induced periodic surface structures (LIPSSs) that can be expanded over large surface areas by scanning the Si surface with a laser beam at a constant scanning speed, preserving a certain number of laser pulses N applied per surface site [35]. An example of such nanoscale morphology produced by scanning the Si surface along a snake-like trajectory (vertical offset between linear scan lines of 0.8 um) at F = 0.1 J/cm^2, a scanning speed v = 0.1 mm/s, and a 1 KHz pulse repetition rate is shown in Figure 1b. At the same time, laser-induced heating of the Si wafer as well as partial heat dissipation to the surrounding solution facilitates thermal decomposition of the $AgNO_3$ precursor to the metal phase. This process is expected to be localized near the laser-heated interface and results in the decoration of the formed surface morphology by Ag nanoparticles with an average size of 30 ± 10 nm that can be seen on the close-up SEM images (inset of Figure 1b). What is noteworthy is that both the multi-photon photoreduction and the plasma-assisted reduction scenario [31,36–38] of $AgNO_3$ decomposition can hardly be realized in our case considering the near-threshold laser fluence F used in this experiment as well as the rather low thermal decomposition temperature (>250 °C) of the metal precursor.

It is important to stress that controllable laser texturing of Si in liquid surroundings substantially limits the range of available laser fluences. In particular, at the fixed ratio between scanning speed v and the pulse repetition rate, an increase in F up to 0.145 J/cm^2 leads to excessive boiling of the functionalizing solution at the interface that deteriorates the focal plane profile of the laser beam near the Si surface resulting in uneven laser nanopatterning. Laser fluence below 0.1 J/cm^2 causes no evident surface modification even at a much higher number of applied pulses N per surface site (much slower scanning speed v). What is noteworthy is that the variation in the fluence within the mentioned optimal processing range $0.1 < F < 0.145$ J/cm^2 for the fixed content of $AgNO_3$ in the functionalizing solution weakly affects the average content of the Ag within the processed area (around 2.2 ± 0.5 wt.% according to the EDX analysis).

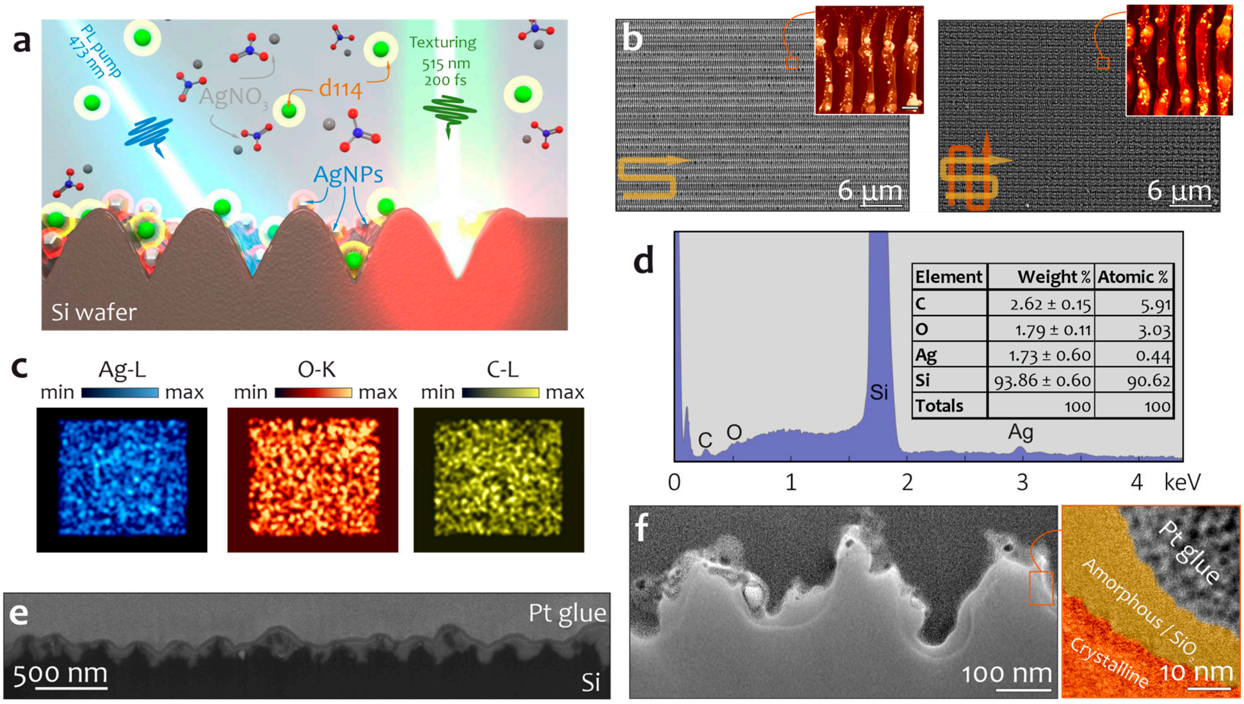

Figure 1. (**a**) Schematically illustrated procedure of SEPL sensor fabrication. (**b**) Top-view SEM images of the laser-patterned Si surface produced under single- (**left**) and double-pass (**right**) procedures. Insets on both images provide a closer look at the surface morphology with well seen isolated Ag nanoparticles. Arrows in the left-bottom part of the images illustrate the laser scanning directions. (**c**) EDX chemical mapping and (**d**) EDX spectrum (the inset table shows elemental composition) of the Si surface containing a square-shaped laser textured area (a lateral size of 50×50 µm^2). (**e**) Averaged height (200–300 nm) and periodicity (around 250 nm) of nano-trenches in the laser-patterned Si surface revealed by an SEM image of a cross-sectional FIB cut made perpendicularly to the trench orientation. (**f**) Close-up TEM images of the Si nano-trenches that show the decorating Ag nanoparticles and the disordered (amorphized or oxidized) Si near-surface layer. A solution containing 10^{-3} M of $AgNO_3$ was used to produce all of the demonstrated surface textures.

Figure 1c,d summarizes the results of the EDX chemical mapping of the Si surface with a central laser-textured area using a solution containing 10^{-3} M $AgNO_3$ and the 10^{-3} M d114 probe. These results clearly indicate localized decoration of the patterned area with Ag nanoparticles and partial oxidation of the surface upon laser texturing, as well as an increased content of carbon atoms in this area. The latter can be related to the local deposition of d114 molecules from the functionalizing solution due to adsorption on a significantly increased area of the patterned surface. Such deposition appears to be stimulated by the good wettability of the laser-textured surface and strong Van der Waals forces acting in the nano-trenches. Figure 1e,f provides deeper insights into the nanoscale morphology and composition of the Ag-decorated Si nano-trenches. In particular, the demonstrated SEM and TEM images reveal the average depth of the trenches (approx. 250 nm), the presence of Ag nanoparticles, and an interface Si layer with a disordered lattice. The latter feature can be attributed to the laser-induced amorphization of silicon upon ultrafast laser heating/recrystallization [39] or the formation of silicon dioxide [23].

To further increase the effective surface area upon laser-texturing of the Si in a functionalizing solution, the processed area was scanned again along the snake-like trajectory, keeping the same experimental parameters (F = 0.1 J/cm^2, v = 0.1 mm/s and 1 KHz pulse repetition; lateral offset between the scan line of 0.8 um; Figure 1f). This process slightly increases the Ag content (up to 2.5 wt.%) and adds a microscale surface morphology to the already created nano-trenches which can be observed by comparing the visible and near-IR reflectance spectra of textures produced under single- and double-pass procedures (Figure 2a,b). First of all, in both cases the average reflectivity drops by more than an order of magnitude compared to the reflectivity of the pristine Si wafer. Moreover, an additional laser pass creates hierarchical surface morphology superimposed with the already produced nanograting, strongly reducing the surface reflectivity at near-IR frequencies and confirming the enlarged surface area. Figure 2c summarizes studies of the various optical properties of a representative patterned Si surface area (a lateral size of 50 × 50 um^2) carried out using confocal laser microspectroscopy at 473 nm pump. Along with a locally reduced surface reflectivity, these studies also reveal enhanced Raman yield associated with the c-Si band at 521 cm^{-1} within the textured surface area as well as a 20-fold more enhanced PL signal (compared to a smooth Si wafer dipped into the same functionalization solution; Figure 2d) related to adsorbed d114 molecules capping such hierarchical morphology. The uniform PL signal coming from these molecules indicates their homogeneous distribution over the textured surface. Both PL and Raman signals are known to be proportional to the pump radiation intensity which is expected to be enhanced owing to reduced reflectivity as well as near-field light localization effects at the pump wavelength. Such effects can be stimulated by micro- and nanostructures formed on the Si surface localizing pump radiation within the near-surface layer and surface plasmons supported by decorating Ag nanoparticles. In addition, in the case of PL signal enhancement, the interaction of quantum emitters (such as organic dye molecules) with optically resonant structures (such as plasmonic nanoparticles or Mie-resonant Si surface features) can also lead to spontaneous emission enhancement via the Purcell effect related to a reduction in the radiative lifetime as well as modification of the emission directivity. Comparison of d114 PL signals collected on smooth and textured surface sites with microscope objectives with NA = 0.7 and 0.28 showed that molecules on a laser-textured surface emit light predominantly in the vertical direction. Along with the discussed Purcell effect, this can also indicate the localization of d114 molecules within the Si nano-trenches owing to Van der Waals forces, as mentioned above.

As mentioned above, a variation in the laser fluence F within a rather narrow optimal processing window weakly affects the amount of Ag nanoparticles decorating the Si surface. At the same time, this amount can be efficiently controlled by tuning the concentration of the $AgNO_3$ precursor in the functionalizing solution. Figure 2e clarifies the role of Ag nanoparticles in the SEPL properties of the produced surface textures. In particular, a low $AgNO_3$ concentration provides a negligibly small amount of decorating plasmonic nanoparticles, resulting in rather weak PL signal enhancement (with respect to those achieved on a patterned Si surface produced in a functionalizing solution without $AgNO_3$) irrespective of the surface morphology controlled by the applied fluence F. An increase in the Ag content provides up to an eight-fold boost in the spontaneous emission from the d114 molecular layer on the laser-patterned surfaces. This feature indicates a strong contribution of plasmon-mediated effects to the observed enhancement of d114 spontaneous emissions evidently dominating over the related PL quenching effects. Efficient interaction of the organic molecules with plasmonic nanoparticles is also obvious from the appearance of the vibration bands related to the d114 organic dye in the optical spectra owing to the surface-enhanced Raman scattering effect (inset, Figure 2d).

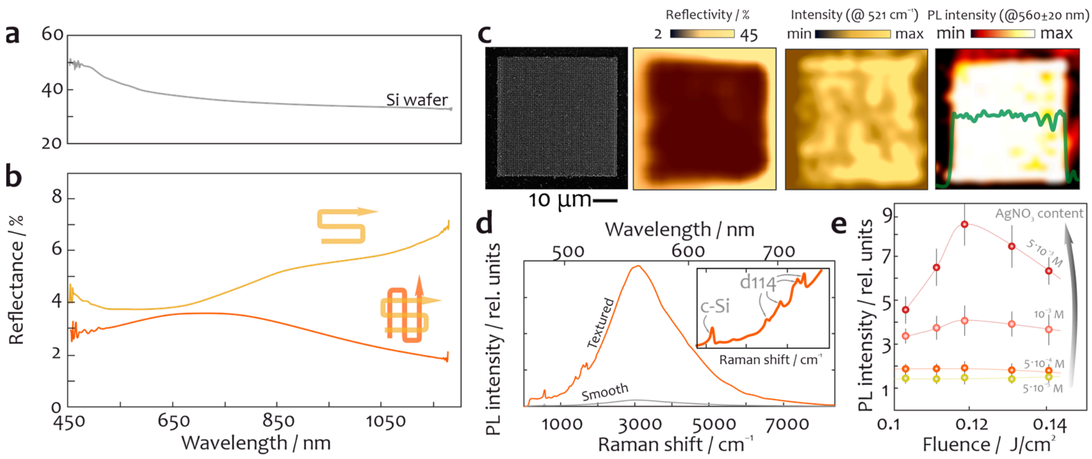

Figure 2. Reflectance spectra of (**a**) the pristine Si wafer and (**b**) the laser-textured Si surface areas produced using either single- or double-pass approaches (in both cases, the fixed laser fluence F = 0.1 J/cm^2 was used). (**c**) Correlated reference SEM, surface reflectivity (at 473 nm), Raman (at 520 $\pm$ cm^{-1}), and PL (at 560 $\pm$ 30 nm) images of the laser-patterned hierarchical surface area. The green curve in the right-most image provides an average PL intensity profile over the textured area and surrounding smooth sites. (**d**) PL spectra of d114 organic dye nanolayer on the laser-patterned (orange curve) and smooth (gray curve) Si surface sites. The inset magnifies the part of the spectrum with well-seen Raman bands of crystalline silicon and d114 organic dye. (**e**) Average normalized PL yield from the d114 layer as a function of laser fluence F used to produce hierarchical Si nanotextures in functionalizing solutions containing variable amounts of $AgNO_3$ ranging from 5×10^{-5} to 5×10^{-3} M. A signal from the laser-patterned Si surface produced in the functionalizing solution without $AgNO_3$ was used for signal normalization.

The produced Ag-decorated hierarchical Si textures functionalized with a light-emitting d114 nano-layer were further tested regarding their ability to detect highly toxic Hg^{2+} ions in water. The utilized molecular probe dissolved in the water/methanol system has previously shown its efficiency regarding the detection of Hg^{2+} via PL yield proportional to ion concentration (Figure 3a). The calibration dependence of d114 solution ($2 \cdot \times 10^{-5}$ M) PL intensity on the Hg^{2+} concentration is shown in Figure 3b, revealing the detection limit of such a PL sensing approach as small as ≈0.01 µM. To attest the sensing performance of laser-patterned textures, the samples were placed into a fluidic device to inject either Hg^{2+} aqueous solution of variable concentrations or EDTA solution to remove chelated ions and restore the sensitive layer (Figure 3c). Due to the efficient laser pump (at 473 nm) of the molecular nanolayer covering the anti-reflecting NP-decorated Si surface morphology that provides good matching of both the NP plasmon band and the emitter absorption band, a stable and detectable PL signal from the sensitive layer was observed even at low-intensity pumping (≈20 µW/µm^2). In addition, the signal stability was also ensured by the poor water solubility of d114, which prevents it from leaching into solution during multiple injections of the deionized water containing trace amounts of Hg^{2+}. The laser-patterned Si sensor reacts by increasing the average PL intensity as a function of mercury ion concentration in the injected liquid as shown in Figure 3d,e. Systematic studies of the device response allowed us to calculate the limit of detection (LoD) as 3σ/slope ~ 100 pM as well as the dynamic range of sensor operation up to ~100 nM. By comparing the LoD value obtained for the patterned Si sensor functionalized by d114 molecules with those achieved in the solution state, one can find at least 100-fold better performance for the SEPL-based approach. Moreover, chelated ions can be rather quickly removed from the sensitive layer by sequentially washing the sample in the EDTA solution and deionized water; as a result the sensor demonstrated reusability and reversibility of the optical response (Figure 3f,g).

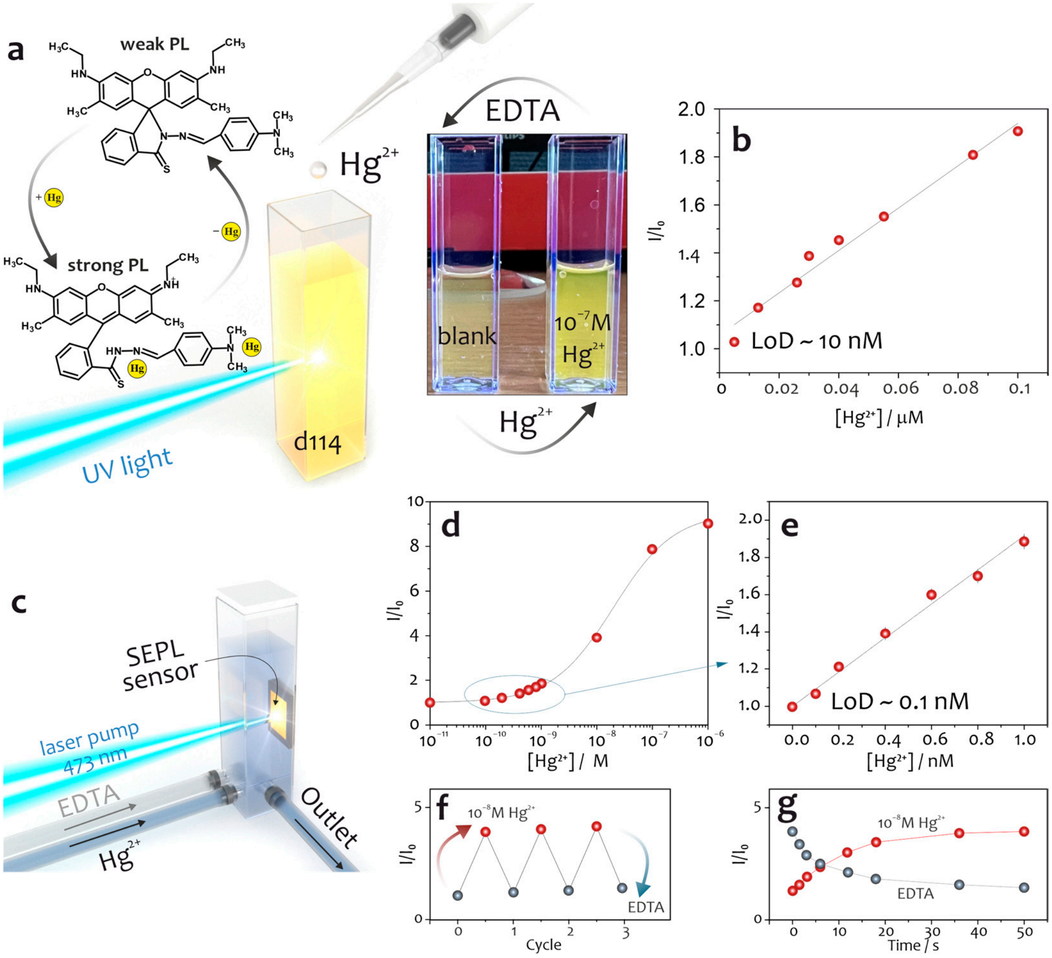

Figure 3. (**a**) Schematic illustration of Hg^{2+} recognition by d114 (left panel) and photograph demonstrating the optical response of the probe in solution under illumination with 365 nm LED (right panel). (**b**) Dependence of the response signal on the analyte concentration and results of the Hg^{2+} LoD calculations. (**c**) Schematic of the experimental setup used for Hg^{2+} optical sensing by the SEPL sensor. (**d**) Wide-range dependence of the response signal on the analyte concentration (10^{-11}–10^{-6} M Hg^{2+}) in log-scale and (**e**) linear range in the region of low concentrations revealing Hg^{2+} LoD. (**f**) Reversibility of the optical response and (**g**) kinetics characteristics of the SEPL sensor.

4. Conclusions

To conclude, an SEPL sensor with outstanding performance regarding the detection of toxic mercury ions was fabricated using single-pot single-step direct fs-laser patterning of a Si wafer in a functionalizing solution. The SEPL effect coming from the efficient light intensity localization by the laser-textured interface containing a light-emitting nanolayer of chemosensory molecules allowed us to reach the detection limit of mercury ions of 100 pM which is two orders of magnitude lower compared to this molecular probe's sensitivity in solution. The fabrication technique is upscalable, inexpensive, and flexible regarding the ability to control the surface nano-morphology of Si [23,27,40–42], the amount and type of loading noble-metal nanoparticles [31,43,44], as well as the type of molecular probe. This opens up pathways for the on-demand development of various multi-functional chemosensing platforms with expanded functionality.

Supplementary Materials: The following supporting information can be downloaded at: https://www.mdpi.com/article/10.3390/chemosensors11050307/s1. Detailed synthesis procedure and Figure S1: The synthesis route of d114 (compound 2); Figure S2: Schematic of the experimental setup for laser assisted fabrication of SEPL sensor.

Author Contributions: Conceptualization, A.K. and A.M.; methodology, S.G. and A.K.; validation, S.G. and M.T.; resources, M.T. and E.M.; formal analysis, M.T., Y.B. and A.C.; investigation, Y.B., A.C. and E.M; data curation, E.M. and Y.B.; writing—original draft preparation, A.K. and A.M.; visualization, A.C. and S.G.; project administration, A.M.; supervision, A.K.; funding acquisition, A.M. All authors have read and agreed to the published version of the manuscript.

Funding: This research was funded by the Russian Science Foundation, grant number 18-79-10091.

Institutional Review Board Statement: Not applicable.

Informed Consent Statement: Not applicable.

Data Availability Statement: The data presented in this study are available from the corresponding author upon request.

Conflicts of Interest: The authors declare no conflict of interest.

References

1. Tutov, M.V.; Sergeev, A.A.; Zadorozhny, P.A.; Bratskaya, S.Y.; Mironenko, A.Y. Dendrimeric Rhodamine Based Fluorescent Probe for Selective Detection of Au. *Sens. Actuators B Chem.* **2018**, *273*, 916–920. [CrossRef]
2. Mironenko, A.Y.; Tutov, M.V.; Sergeev, A.A.; Voznesenskiy, S.S.; Bratskaya, S.Y. On/off Rhodamine Based Fluorescent Probe for Detection of Au and Pd in Aqueous Solutions. *Sens. Actuators B Chem.* **2017**, *246*, 389–394. [CrossRef]
3. Tutov, M.V.; Sergeev, A.A.; Shamich, N.I.; Chepak, A.K.; Mironenko, A.Y. Synthesis and Optical Properties of Rhodamine Terminated Organosilicon Dendrimers. *Dye. Pigment.* **2021**, *184*, 108783. [CrossRef]
4. Mironenko, A.Y.; Tutov, M.V.; Chepak, A.K.; Zadorozhny, P.A.; Bratskaya, S.Y. A Novel Rhodamine-Based Turn-on Probe for Fluorescent Detection of Au^{3+} and Colorimetric Detection of Cu^{2+}. *Tetrahedron* **2019**, *75*, 1492–1496. [CrossRef]
5. Wang, L.; Ding, H.; Ran, X.; Tang, H.; Cao, D. Recent Progress on Reaction-Based BODIPY Probes for Anion Detection. *Dye. Pigment.* **2020**, *172*, 107857. [CrossRef]
6. La, M.; Hao, Y.; Wang, Z.; Han, G.-C.; Qu, L. Selective and Sensitive Detection of Cyanide Based on the Displacement Strategy Using a Water-Soluble Fluorescent Probe. *J. Anal. Methods Chem.* **2016**, *2016*, 1462013. [CrossRef] [PubMed]
7. Wu, L.; Sedgwick, A.C.; Sun, X.; Bull, S.D.; He, X.-P.; James, T.D. Reaction-Based Fluorescent Probes for the Detection and Imaging of Reactive Oxygen, Nitrogen, and Sulfur Species. *Acc. Chem. Res.* **2019**, *52*, 2582–2597. [CrossRef]
8. Nguyen, V.N.; Ha, J.; Cho, M.; Li, H.; Swamy, K.M.K.; Yoon, J. Recent Developments of BODIPY-Based Colorimetric and Fluorescent Probes for the Detection of Reactive Oxygen/Nitrogen Species and Cancer Diagnosis. *Coord. Chem. Rev.* **2021**, *439*, 213936. [CrossRef]
9. Melnychuk, N.; Egloff, S.; Runser, A.; Reisch, A.; Klymchenko, A.S. Light-Harvesting Nanoparticle Probes for FRET-Based Detection of Oligonucleotides with Single-Molecule Sensitivity. *Angew. Chemie Int. Ed.* **2020**, *59*, 6811–6818. [CrossRef] [PubMed]
10. Jurek, K.; Kabatc, J.; Kostrzewska, K.; Grabowska, M. New Fluorescence Probes for Biomolecules. *Molecules* **2015**, *20*, 13071–13079. [CrossRef]
11. Gao, S.; Zhou, R.; Samanta, S.; Qu, J.; Ohulchanskyy, T.Y. Recent Advances in Plasmon-Enhanced Luminescence for Biosensing and Bioimaging. *Anal. Chim. Acta* **2023**, *1254*, 341086. [CrossRef]
12. Larson, D.R.; Zipfel, W.R.; Williams, R.M.; Clark, S.W.; Bruchez, M.P.; Wise, F.W.; Webb, W.W. Water-Soluble Quantum Dots for Multiphoton Fluorescence Imaging in vivo. *Science* **2003**, *300*, 1434–1436. [CrossRef]
13. Zhang, Y.; Zhang, L.; Yang, L.; Vong, C.I.; Chan, K.F.; Wu, W.K.K.; Kwong, T.N.Y.; Lo, N.W.S.; Ip, M.; Wong, S.H.; et al. Real-Time Tracking of Fluorescent Magnetic Spore–Based Microrobots for Remote Detection of C. Diff Toxins. *Sci. Adv.* **2019**, *5*, eaau9650. [CrossRef]
14. Feng, X.; Liu, L.; Wang, S.; Zhu, D. Water-Soluble Fluorescent Conjugated Polymers and Their Interactions with Biomacromolecules for Sensitive Biosensors. *Chem. Soc. Rev.* **2010**, *39*, 2411. [CrossRef]
15. Zhu, C.; Liu, L.; Yang, Q.; Lv, F.; Wang, S. Water-Soluble Conjugated Polymers for Imaging, Diagnosis, and Therapy. *Chem. Rev.* **2012**, *112*, 4687–4735. [CrossRef]
16. Bouhedda, F.; Fam, K.T.; Collot, M.; Autour, A.; Marzi, S.; Klymchenko, A.; Ryckelynck, M. A Dimerization-Based Fluorogenic Dye-Aptamer Module for RNA Imaging in Live Cells. *Nat. Chem. Biol.* **2020**, *16*, 69–76. [CrossRef]
17. Farzan, V.M.; Kvach, M.V.; Aparin, I.O.; Kireev, D.E.; Prikazchikova, T.A.; Ustinov, A.V.; Shmanai, V.V.; Shipulin, G.A.; Korshun, V.A.; Zatsepin, T.S. Novel Homo Yin-Yang Probes Improve Sensitivity in RT-QPCR Detection of Low Copy HIV RNA. *Talanta* **2019**, *194*, 226–232. [CrossRef]
18. Mironenko, A.Y.; Tutov, M.V.; Chepak, A.K.; Bratskaya, S.Y. FRET Pumping of Rhodamine-Based Probe in Light-Harvesting Nanoparticles for Highly Sensitive Detection of Cu^{2+}. *Anal. Chim. Acta* **2022**, *1229*, 340388. [CrossRef]
19. Chepak, A.; Balatskiy, D.; Tutov, M.; Mironenko, A.; Bratskaya, S. Light Harvesting Nanoprobe for Trace Detection of Hg^{2+} in Water. *Molecules* **2023**, *28*, 1633. [CrossRef]

20. Sergeeva, K.A.; Tutov, M.V.; Zhizhchenko, A.Y.; Cherepakhin, A.B.; Leonov, A.A.; Chepak, A.K.; Mironenko, A.Y.; Sergeev, A.A. Ordered Photonic Nanojet Arrays for Luminescent Optical Sensing in Liquid and Gaseous Media. *Sens. Actuators B Chem.* **2023**, *381*, 133435. [CrossRef]
21. Bratskaya, S.; Sergeeva, K.; Konovalova, M.; Modin, E.; Svirshchevskaya, E.; Sergeev, A.; Mironenko, A.; Pestov, A. Ligand-Assisted Synthesis and Cytotoxicity of ZnSe Quantum Dots Stabilized by N-(2-Carboxyethyl) chitosans. *Colloids Surf. B Biointerfaces* **2019**, *182*, 110342. [CrossRef]
22. Kümmerlen, J.; Leitner, A.; Brunner, H.; Aussenegg, F.R.; Wokaun, A. Enhanced Dye Fluorescence over Silver Island Films: Analysis of the Distance Dependence. *Mol. Phys.* **1993**, *80*, 1031–1046. [CrossRef]
23. Dostovalov, A.; Bronnikov, K.; Korolkov, V.; Babin, S.; Mitsai, E.; Mironenko, A.; Tutov, M.; Zhang, D.; Sugioka, K.; Maksimovic, J.; et al. Hierarchical Anti-Reflective Laser-Induced Periodic Surface Structures (LIPSSs) on Amorphous Si Films for Sensing Applications. *Nanoscale* **2020**, *12*, 13431–13441. [CrossRef] [PubMed]
24. Borodaenko, Y.; Gurbatov, S.; Tutov, M.; Zhizhchenko, A.; Kulinich, S.A.; Kuchmizhak, A.; Mironenko, A. Direct Femtosecond Laser Fabrication of Chemically Functionalized Ultra-Black Textures on Silicon for Sensing Applications. *Nanomaterials* **2021**, *11*, 401. [CrossRef] [PubMed]
25. Mironenko, A.Y.; Tutov, M.V.; Sergeev, A.A.; Mitsai, E.V.; Ustinov, A.Y.; Zhizhchenko, A.Y.; Linklater, D.P.; Bratskaya, S.Y.; Juodkazis, S.; Kuchmizhak, A.A. Ultratrace Nitroaromatic Vapor Detection via Surface-Enhanced Fluorescence on Carbazole-Terminated Black Silicon. *ACS Sens.* **2019**, *4*, 2879–2884. [CrossRef]
26. Sergeeva, K.A.; Tutov, M.V.; Voznesenskiy, S.S.; Shamich, N.I.; Mironenko, A.Y.; Sergeev, A.A. Highly-Sensitive Fluorescent Detection of Chemical Compounds via Photonic Nanojet Excitation. *Sens. Actuators B Chem.* **2020**, *305*, 127354. [CrossRef]
27. Borodaenko, Y.; Khairullina, E.; Levshakova, A.; Shmalko, A.; Tumkin, I.; Gurbatov, S.; Mironenko, A.; Mitsai, E.; Modin, E.; Gurevich, E.L.; et al. Noble-Metal Nanoparticle-Embedded Silicon Nanogratings via Single-Step Laser-Induced Periodic Surface Structuring. *Nanomaterials* **2023**, *13*, 1300. [CrossRef]
28. Taylor, A.B.; Zijlstra, P. Single-Molecule Plasmon Sensing: Current Status and Future Prospects. *ACS Sens.* **2017**, *2*, 1103–1122. [CrossRef]
29. Jiang, R.; Li, B.; Fang, C.; Wang, J. Metal/Semiconductor Hybrid Nanostructures for Plasmon-Enhanced Applications. *Adv. Mater.* **2014**, *26*, 5274–5309. [CrossRef]
30. Fusco, Z.; Rahmani, M.; Tran-Phu, T.; Ricci, C.; Kiy, A.; Kluth, P.; Della Gaspera, E.; Motta, N.; Neshev, D.; Tricoli, A. Photonic Fractal Metamaterials: A Metal–Semiconductor Platform with Enhanced Volatile-Compound Sensing Performance. *Adv. Mater.* **2020**, *32*, 2002471. [CrossRef]
31. Borodaenko, Y.; Syubaev, S.; Khairullina, E.; Tumkin, I.; Gurbatov, S.; Mironenko, A.; Mitsai, E.; Zhizhchenko, A.; Modin, E.; Gurevich, E.L.; et al. On-Demand Plasmon Nanoparticle-Embedded Laser-Induced Periodic Surface Structures (LIPSSs) on Silicon for Optical Nanosensing. *Adv. Opt. Mater.* **2022**, *10*, 2201094. [CrossRef]
32. Gurbatov, S.O.; Modin, E.; Puzikov, V.; Tonkaev, P.; Storozhenko, D.; Sergeev, A.; Mintcheva, N.; Yamaguchi, S.; Tarasenka, N.N.; Chuvilin, A.; et al. Black Au-Decorated TiO_2 Produced via Laser Ablation in Liquid. *ACS Appl. Mater. Interfaces* **2021**, *13*, 6522–6531. [CrossRef]
33. Zuev, D.A.; Makarov, S.V.; Mukhin, I.S.; Milichko, V.A.; Starikov, S.V.; Morozov, I.A.; Shishkin, I.I.; Krasnok, A.E.; Belov, P.A. Fabrication of Hybrid Nanostructures via Nanoscale Laser-Induced Reshaping for Advanced Light Manipulation. *Adv. Mater.* **2016**, *28*, 3087–3093. [CrossRef]
34. Borodaenko, Y.; Syubaev, S.; Gurbatov, S.; Zhizhchenko, A.; Porfirev, A.; Khonina, S.; Mitsai, E.; Gerasimenko, A.V.; Shevlyagin, A.; Modin, E.; et al. Deep Subwavelength Laser-Induced Periodic Surface Structures on Silicon as a Novel Multifunctional Biosensing Platform. *ACS Appl. Mater. Interfaces* **2021**, *13*, 54551–54560. [CrossRef]
35. Bonse, J.; Gräf, S. Maxwell Meets Marangoni—A Review of Theories on Laser-Induced Periodic Surface Structures. *Laser Photon. Rev.* **2020**, *14*, 2000215. [CrossRef]
36. Broadhead, E.J.; Tibbetts, K.M. Fabrication of Gold–Silicon Nanostructured Surfaces with Reactive Laser Ablation in Liquid. *Langmuir* **2020**, *36*, 10120–10129. [CrossRef]
37. Ran, P.; Jiang, L.; Li, X.; Li, B.; Zuo, P.; Lu, Y. Femtosecond Photon-Mediated Plasma Enhances Photosynthesis of Plasmonic Nanostructures and Their SERS Applications. *Small* **2019**, *15*, 1804899. [CrossRef]
38. Li, C.; Hu, J.; Jiang, L.; Xu, C.; Li, X.; Gao, Y.; Qu, L. Shaped Femtosecond Laser Induced Photoreduction for Highly Controllable Au Nanoparticles Based on Localized Field Enhancement and Their SERS Applications. *Nanophotonics* **2020**, *9*, 691–702. [CrossRef]
39. Garcia-Lechuga, M.; Puerto, D.; Fuentes-Edfuf, Y.; Solis, J.; Siegel, J. Ultrafast Moving-Spot Microscopy: Birth and Growth of Laser-Induced Periodic Surface Structures. *ACS Photonics* **2016**, *3*, 1961–1967. [CrossRef]
40. Zhang, D.; Ranjan, B.; Tanaka, T.; Sugioka, K. Underwater Persistent Bubble-Assisted Femtosecond Laser Ablation for Hierarchical Micro/Nanostructuring. *Int. J. Extrem. Manuf.* **2020**, *2*, 015001. [CrossRef]
41. Zhang, D.; Sugioka, K. Hierarchical Microstructures with High Spatial Frequency Laser Induced Periodic Surface Structures Possessing Different Orientations Created by Femtosecond Laser Ablation of Silicon in Liquids. *Opto-Electron. Adv.* **2019**, *2*, 19000201–19000218. [CrossRef]
42. Allahyari, E.; Nivas, J.J.; Skoulas, E.; Bruzzese, R.; Tsibidis, G.D.; Stratakis, E.; Amoruso, S. On the Formation and Features of the Supra-Wavelength Grooves Generated during Femtosecond Laser Surface Structuring of Silicon. *Appl. Surf. Sci.* **2020**, *528*, 146607. [CrossRef]

43. Kay, K.E.; Batista, L.M.F.; Tibbetts, K.M.; Ferri, J.K. Stability of Uncapped Gold Nanoparticles Produced via Laser Reduction in Liquid. *Colloids Surf. A Physicochem. Eng. Asp.* **2022**, *652*, 129860. [CrossRef]
44. Frias Batista, L.M.; Kunzler, K.; John, M.G.; Clark, B.; Bullock, A.; Ferri, J.; Gupton, B.F.; Tibbetts, K.M. Laser Synthesis of Uncapped Palladium Nanocatalysts. *Appl. Surf. Sci.* **2021**, *557*, 149811. [CrossRef]